nature climate change

Supplementary information

https://doi.org/10.1038/s41558-026-02620-1

Atmospheric warming contributions from airborne microplastics and nanoplastics

In the format provided by the authors and unedited

Table of contents

Supplementary Discussion

Optical Properties of ageing MNPs

Atmospheric ageing markedly modifies the optical properties of MNPs. Using a custom flow-tube reactor to simulate photochemical oxidation, we observed that white MNPs underwent pronounced yellowing, as reflected by a marked increase in their imaginary RI (k) at 550 nm from ~0.005 to ~0.26—comparable to that of pristine yellow MNPs (Fig. S10). This enhancement in visible-light absorption is possibly attributed to photo-oxidation via Norrish I/II reactions, which introduce oxygenated functional groups (e.g., vinyl, esters, aldehydes, ketones) that facilitate chromophore formation[1,2]. Intriguingly, the ageing behaviour of red MNPs exhibited a distinct size dependence. Particles with a size of ~500 nm underwent a pronounced "bleaching" effect, characterized by a drop in the imaginary refractive index (k) at 550 nm to nearly zero (Extended Data Fig. 5a). In contrast, similarly composed red particles with a smaller size of ~50 nm showed a trend toward "yellowing", marked by a decline in visible-light absorption at wavelengths beyond 780 nm (Extended Data Fig. 5b). These optical transitions were absent in larger red particles (~5 μm), which can be attributed to their lower specific surface area restricting surface-driven photochemistry, combined with reduced UV penetration into coarser particles that further slows pigment degradation[3]. By contrast, blue, yellow, and black MNPs displayed no notably optical changes under the experimental ageing period, suggesting slower transformation kinetics[4]. Such scenario is driven by the chemical makeup of the red dyes, mainly composed of azo compounds, whose structures are vulnerable to light-induced photo-oxidative degradation and consequent bleaching[4,5].

Distribution of MNPs in the Global Atmosphere

Terrestrial MNP concentrations generally track global patterns of plastic production and consumption, with elevated values occurring in densely populated and industrialized regions, including eastern North America, Central/Western European urban corridors, East Asian manufacturing hubs, and along the African Mediterranean coast. Notably, localized atmospheric pollution hotspots emerge in sub-Saharan regions (e.g., Sudan and Central Africa), reflecting rapid urbanization compounded by insufficient plastic waste management infrastructure[6-8]. Over the ocean, surface MNP concentration distributions align markedly with subtropical convergence zones shaped by Ekman transport and geostrophic circulation, mirroring patterns of sea surface plastic accumulation. Conversely, minimal atmospheric concentrations occur in areas characterized by divergent surface flows, such as North Pacific

subpolar gyre and equatorial current system[7]. Enhanced MNPs' loading averagely within the marine atmospheric boundary layer above the five subtropical garbage patches underscore vigorous air-sea exchange processes, as UV/Vis-photolyzed and mechanically fragmented secondary MNPs undergo aerosolization via sea salt carriers[6-8]. This mechanism is supported by the recent field measurements reporting NP concentrations in surface waters of the North Atlantic gyre of up to ~18.1 mg m^{-3}, substantially exceeding background concentrations across the global ocean[9]. On an annual mean basis, the tropospheric enrichment zone over the North Pacific Subtropical Gyre—commonly referred to as the "Great Pacific Garbage Patch"—exhibits extreme atmospheric MNPs enrichment. Near-surface (< 100 m above ground level) simulated concentrations here reach peak values of ~1.15×10^3 MP m^{-3} for MPs and ~2.67×10^2 ng m^{-3} for NPs, approximately three orders of magnitude above the global background. These maxima underscore the importance of wind-driven vertical transport as the dominant redistribution pathway. Correspondingly, column mass loadings in this region are substantially elevated, with MP loadings typically around ~15.2 mg m^{-2} and NP loadings up to ~1.19 mg m^{-2}. Globally, atmospheric MNPs exhibit marked hemispheric asymmetry, with concentrations in the Northern Hemisphere exceeding those in the Southern Hemisphere by approximately an order of magnitude, driven by emission gradients and prevailing tropospheric circulation.

AOD and AAOD of Global Atmospheric MNPs

For validation, we compared our model results for BC against established benchmarks. The simulated global mean BC AOD is 1.7×10^{-3}, which falls within the multi-model range ($(1.0–2.0) \times 10^{-3}$) reported in the IPCC AR6, confirming that the model realistically captures aerosol optical loading[10-12]. The AOD and AAOD of atmospheric MNPs are strongly influenced by particle colour and size (Tables 1 and 2). Annually averaged at $\lambda = 550$ nm, NPs exhibit an AOD of ~1.1×10^{-4} and an AAOD of ~5.6×10^{-5}—values higher than those for MPs (AOD ~1.5×10^{-5}, AAOD ~6.0×10^{-6})—indicating a greater radiative efficiency per unit mass for the smaller particles (Fig S6). Although the global AOD from MNPs remains about an order of magnitude lower than that of BC, their radiative impact is non-negligible and becomes considerable in regions with high MNP loading. Over the North Pacific Garbage Patch, for example, satellite retrievals from the Ozone Monitoring Instrument (OMAERUV) report an AAOD of ~0.02, well above the global background. Our simulations for the same region

yield an MNP-induced AAOD of ~0.004, which, while also elevated relative to the background, represents about 20 % of the satellite-retrieved signal[13]. Similar localized AAOD enhancements are evident in the OMAERUV data over other major oceanic garbage patches, consistent with the spatial absorption patterns predicted by our MNP simulations.

Seasonal DRF of Global Atmospheric MNPs

Seasonal analysis reveals pronounced monthly variability in MNPs' DRF, with values of approximately 0.035 W m^{-2} (January-March), 0.045 W m^{-2} (April-June), 0.043 W m^{-2} (July-September), and 0.033 W m^{-2} (October-December) (Fig. S7). This monthly variability is primarily driven by changes in solar irradiance. The polar DRF dynamics provide strong support for this mechanism: during April–June, the Arctic DRF peaks near 0.099 W m^{-2}, while Antarctic forcing remains minimal (~0.001 W m^{-2}); from October to December, the pattern reverses (Arctic: ~0.003 W m^{-2}; Antarctic: ~0.018 W m^{-2}). This opposite seasonality closely follows hemispheric differences in solar insolation, where higher summer irradiance increases the direct light-absorption efficiency of MNPs. The consistent relationship between polar DRF extremes and variations in solar zenith angle confirms that incident solar radiation is a key factor regulating plastic–climate interactions across latitudes.

Table S1.

The optical parameters of the MNPs achieved their final environmental aging level and the light-absorbing carbonaceous aerosols, calculated for λ = 550 nm.

	N = n – k*i*	MAC ($m^2\ g^{-1}$)	MEC ($m^2\ g^{-1}$)	burden ($mg\ m^{-2}$)	AAOD (10^{-3})	AOD (10^{-3})	DRF ($W\ m^{-2}$) (all-sky)	DRF ($W\ m^{-2}$) (clear-sky)
MPs	1.48 – 0.22*i*	0.085	0.194	0.075	0.006	0.015	0.006	0.003
NPs	1.48 – 0.22i	3.76	6.33	0.017	0.063	0.109	0.033	0.013
BC[14]			10.5	0.14		1.5	0.18	
"Tar balls"[15]	1.27-0.27*i*	3.85	7.3					
Soot carbon[15]	1.95-0.79*i*	4.55	5.9					
Black BrC[16]	1.31-0.13*i*	1.01						

Table S2.

Optical properties at 550 nm, atmospheric burden, and DRF for aged MPs.

MPs	N = n – k*i*	MAC ($m^2\ g^{-1}$)	MEC ($m^2\ g^{-1}$)	*g* (1)	burden ($mg\ m^{-2}$)	AAOD (10^{-3})	AOD (10^{-3})	DRF ($W\ m^{-2}$) (all-sky)	DRF ($W\ m^{-2}$) (clear-sky)
White	1.61 – 0.08*i*	0.088	0.195	0.94	0.075	0.007	0.015	0.003	0.001
Blue	1.39 – 0.25*i*	0.092	0.194	0.95	0.075	0.007	0.015	0.008	0.004
Red	1.48 – 0.14*i*	0.092	0.195	0.95	0.075	0.007	0.015	0.005	0.003
Yellow	1.45 – 0.26*i*	0.091	0.194	0.95	0.075	0.007	0.015	0.007	0.003
Black	1.53 – 0.32*i*	0.09	0.194	0.93	0.075	0.007	0.015	0.009	0.005
Mean		0.085	0.194	0.93	0.075	0.006	0.015	0.006	0.003
Stddev		0.015	0.001	0.02		0.001	0.001	0.002	0.002

Table S3.

Optical properties at 550 nm, atmospheric burden, and DRF for aged NPs.*

NPs	N = n – k*i*	MAC ($m^2\ g^{-1}$)	MEC ($m^2\ g^{-1}$)	*g* (1)	burden ($mg\ m^{-2}$)	AAOD (10^{-3})	AOD (10^{-3})	DRF ($W\ m^{-2}$) (all-sky)	DRF ($W\ m^{-2}$) (clear-sky)
	1.61 – 0.08*i*	1.69	3.64	0.19	0.012	0.020	0.044	0.010	0.004
White	1.61 – 0.08*i*	1.99	6.06	0.43	0.022	0.044	0.133	0.016	0.008
	1.61 – 0.08*i*	2.02	6.31	0.47	0.017	0.034	0.107	0.014	0.006
	1.39 – 0.25*i*	4.88	6.05	0.19	0.012	0.059	0.073	0.025	0.011
Blue	1.39 – 0.25*i*	4.40	6.6	0.45	0.022	0.097	0.145	0.051	0.019
	1.39 – 0.25*i*	4.20	6.52	0.51	0.017	0.071	0.111	0.046	0.017
	1.48 – 0.14*i*	2.86	4.07	0.19	0.012	0.034	0.049	0.014	0.006
Red	1.48 – 0.14*i*	2.91	5.49	0.44	0.022	0.064	0.121	0.028	0.009
	1.48 – 0.14*i*	2.86	5.64	0.50	0.017	0.049	0.096	0.023	0.008
	1.45 – 0.26*i*	5.00	6.13	0.19	0.012	0.060	0.074	0.021	0.009
Yellow	1.45 – 0.26*i*	4.47	6.58	0.45	0.022	0.098	0.145	0.046	0.015
	1.45 – 0.26*i*	4.26	6.49	0.51	0.017	0.072	0.110	0.041	0.013
	1.53 – 0.32*i*	5.77	7.54	0.2	0.012	0.069	0.090	0.029	0.014
Black	1.53 – 0.32*i*	5.14	8.04	0.45	0.022	0.113	0.177	0.058	0.024
	1.53 – 0.32*i*	4.87	7.83	0.51	0.017	0.083	0.133	0.050	0.021
Mean		3.76	6.33	0.38	0.017	0.065	0.107	0.031	0.012
Stddev		1.93	1.24	0.13	0.005	0.026	0.037	0.016	0.006

* Each colour of NPs is represented by three different sizes, listed from top to bottom as follows: ((d_g, σ_g) = (100 nm, 2), (250 nm, 3), and (400 nm, 4)).

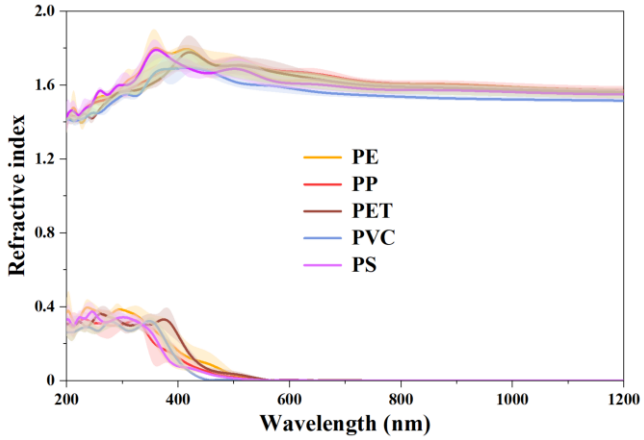

Fig. S1.

The complex refractive indices of pristine polymer MNPs with different type. The mean *n* and *k* values derived from EELS, were plotted against the optical wavelength range of 200 to 1200 nm for the analysed MNPs. The shaded regions represent the standard deviations.

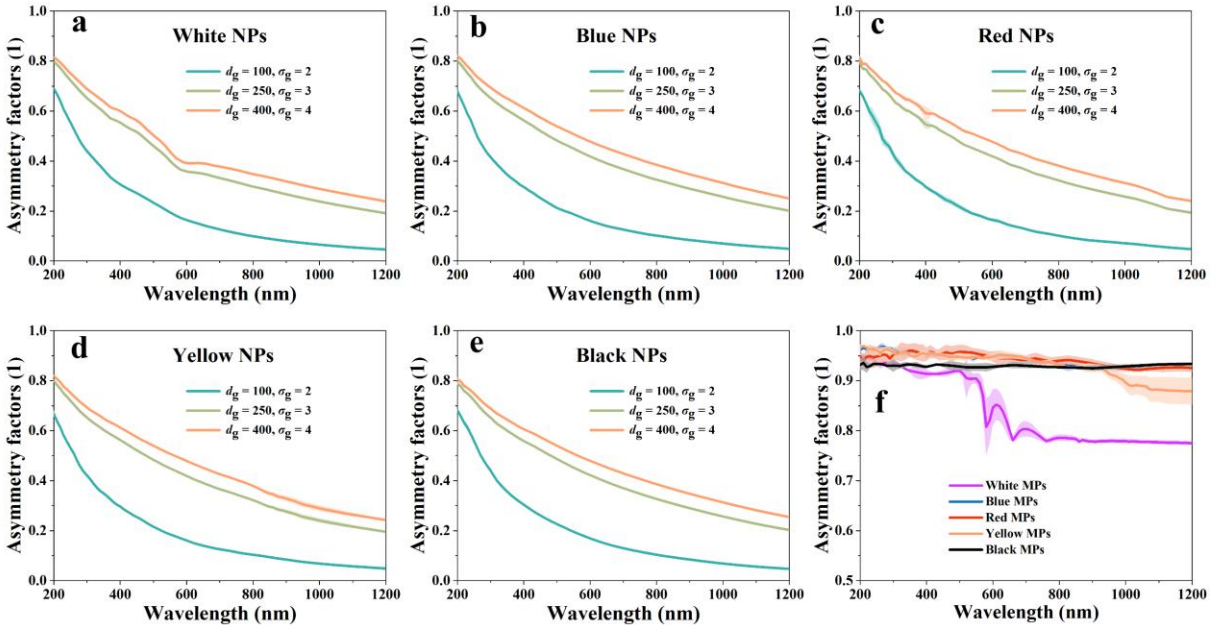

Fig. S2.

Asymmetry factors of airborne MNPs. a-e, Asymmetry factors of (a) white, (b) blue, (c) red, (d) yellow, and (e) black NPs under three log-normal distributions. **f**, Asymmetry factors of MPs with different colors under Gamma size distributions with the shape parameter of 2 and scale parameter 15 μm. The shaded regions represent the standard deviations, based on the analysis of 40 particles for each individual group defined by colour and polymer type (PS, PE, PET), with target sizes following a logarithmic distribution to ensure uniform sampling in log-space. All data are presented as mean values ± standard deviations.

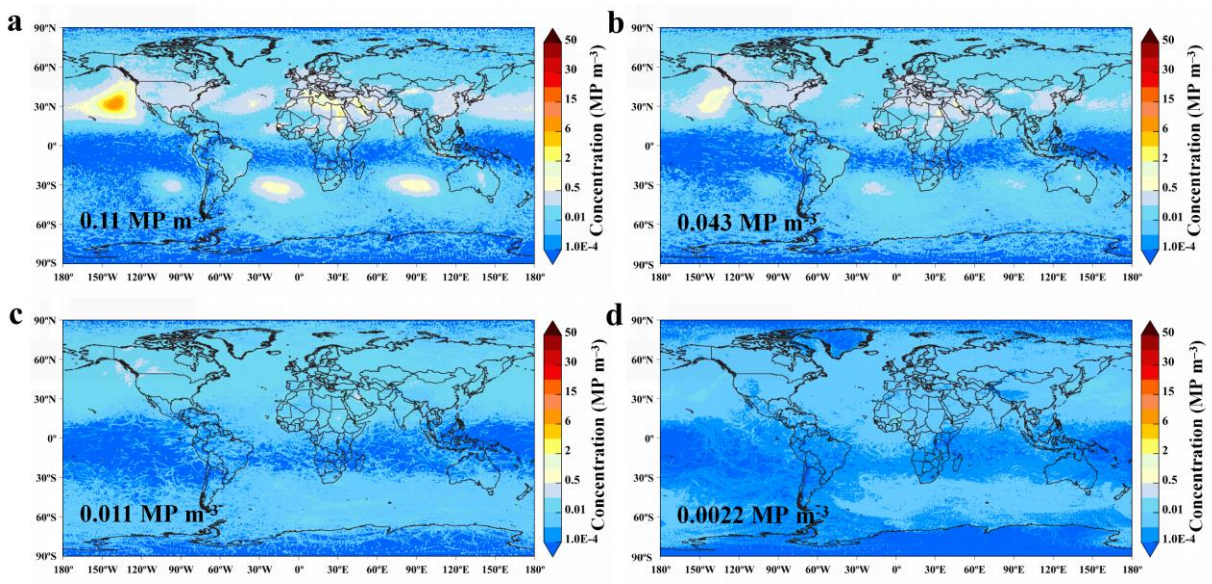

Fig. S3.

Annual mean distribution of MP concentrations at different altitudes. The maps illustrate the global distribution of MP concentrations at heights of (**a**) 1000 m, (**b**) 2000 m, (**c**) 5000 m, (**d**) 10000 m, respectively. The numbers in each panel represent the annual mean MP concentrations (MP m^{-3}) at the corresponding altitude.

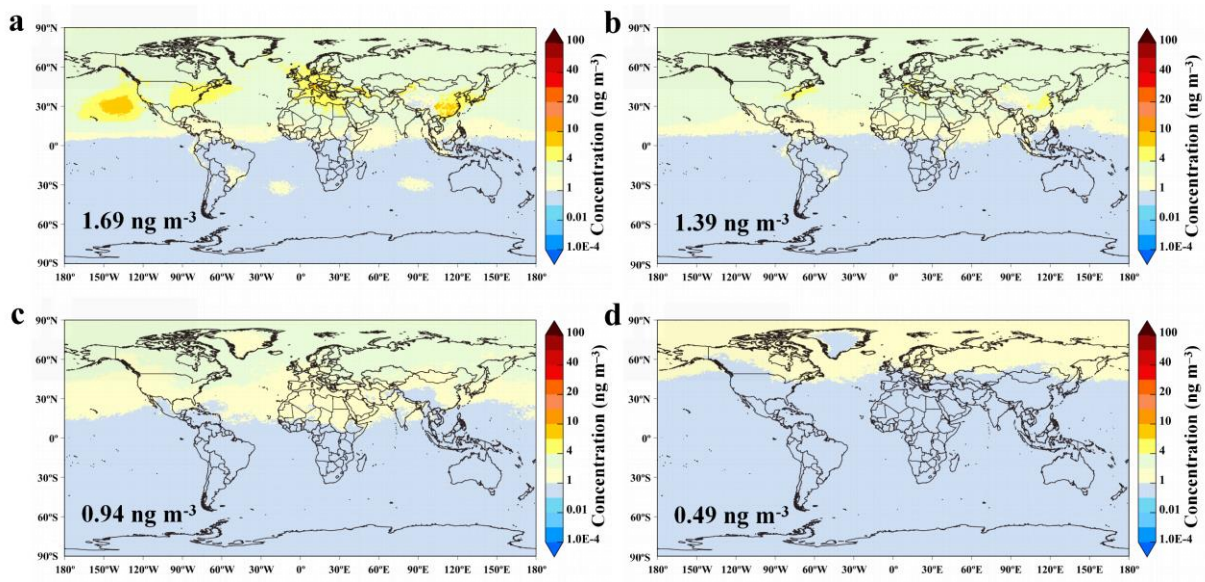

Fig. S4.

Annual mean distribution of NP concentrations at different altitudes. The maps illustrate the global distribution of NP mass concentrations at heights of (**a**) 1000 m, (**b**) 2000 m, (**c**) 5000 m, (**d**) 10000 m, respectively. The numbers in each panel represent the global mean NP mass concentrations (ng m^{-3}) at the corresponding altitude.

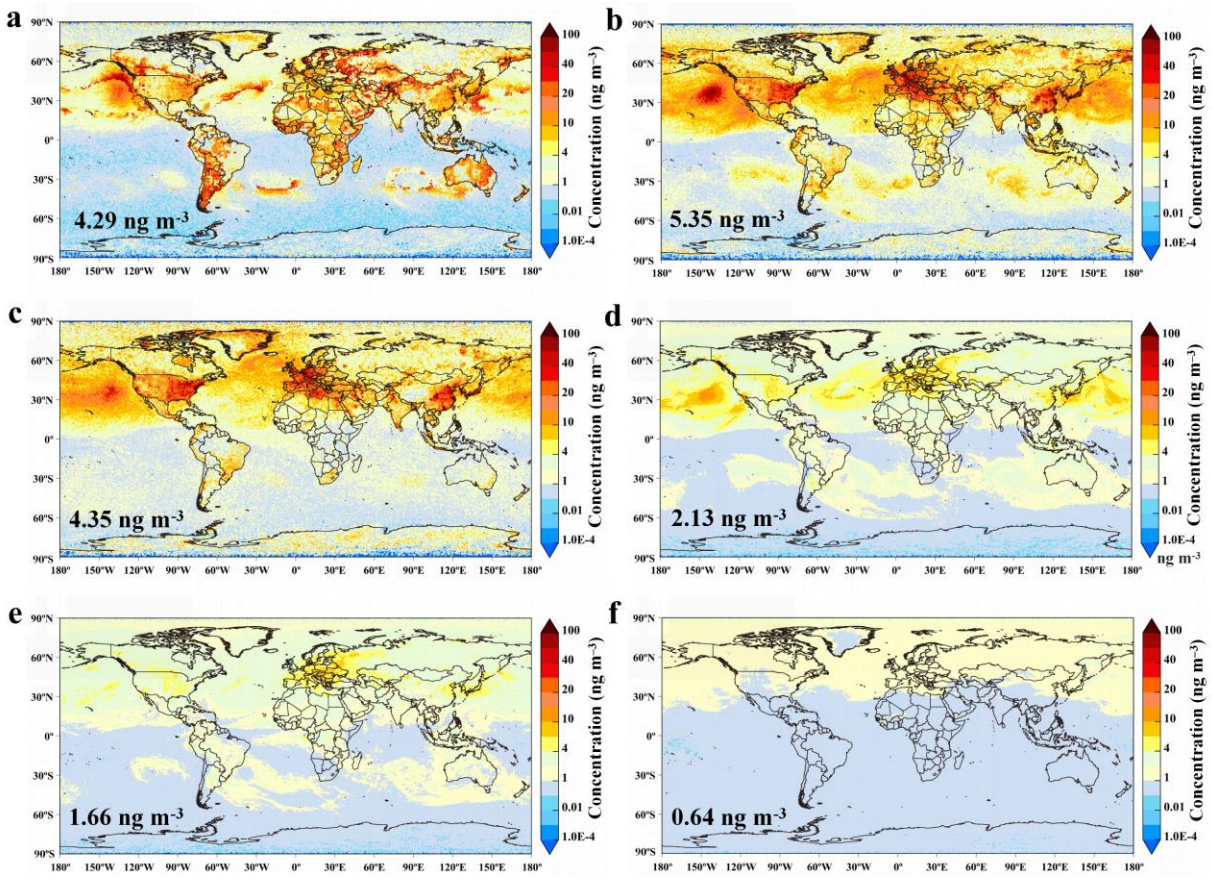

Fig. S5.

Global dispersion of atmospherically NPs modulated by Super Typhoon Mawar. a-c, NP mass concentrations at <100 m altitude during three 10-day typhoon phases: **(a)** pre-typhoon (10–19 May 2023), (**b**) intensification (20–29 May 2023), and (**c**) post-typhoon (30 May–8 Jun 2023). **d-f**, Vertical stratification of NP concentrations at 1,000 m (**d**), 2,000 m (**e**), and 10,000 m (**f**) altitudes. Cyclonic circulation from Super Typhoon Mawar (20 May–2 June 2023) amplified long-range NPs transport.

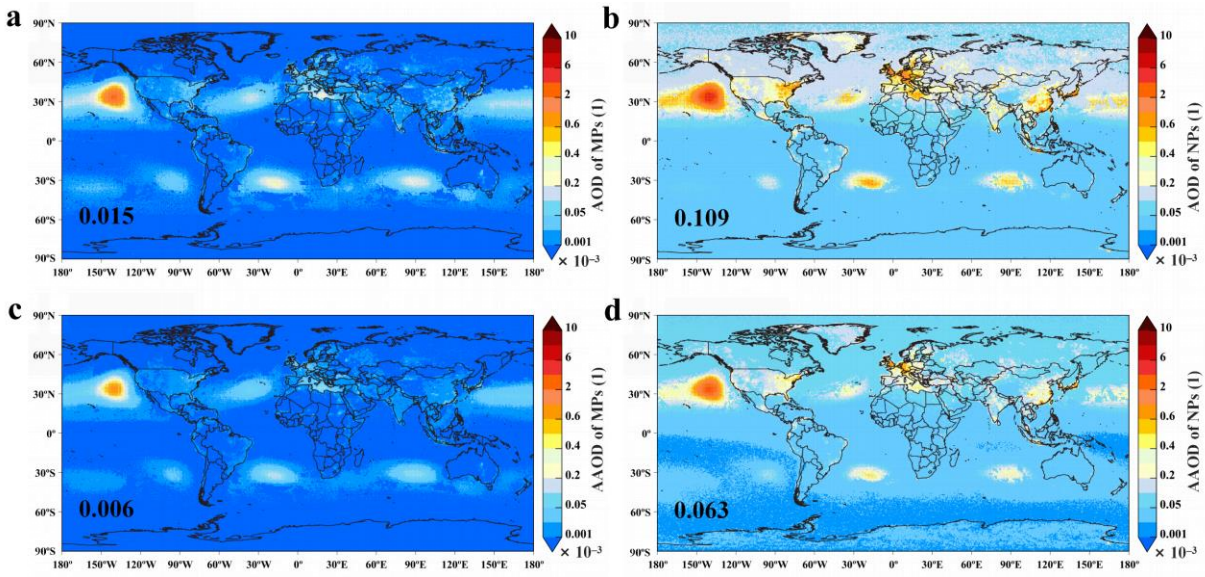

Fig. S6.

Annual mean global distribution of MNPs' AOD and AAOD at 550 nm. a,**b**, The AOD distribution of (**a**) MPs and (**b**) NPs. **c**,**d**, The AAOD distribution of (**c**) MPs and (**d**) NPs. The numerical values in each panel denote the corresponding annual mean.

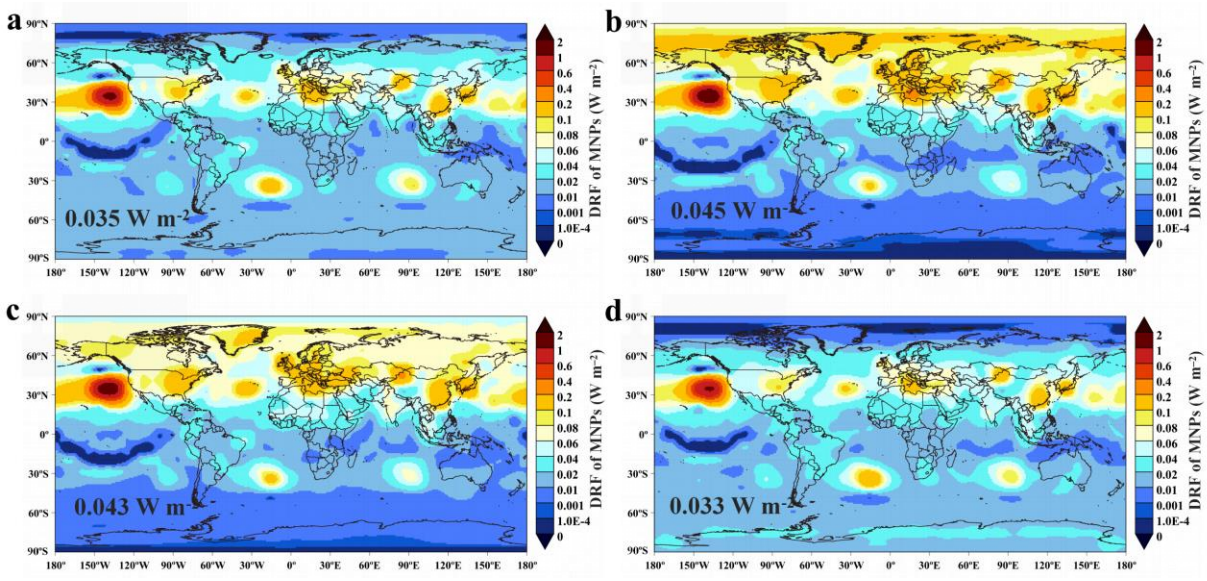

Fig. S7.

Seasonal distribution of atmospheric MNPs' DRF. Panels show global DRF (W m^{-2}) for different seasons: (**a**) January–March, (**b**) April–June, (**c**) July–September, and (**d**) October–December. The numbers in each panel represent the global seasonal mean DRF.

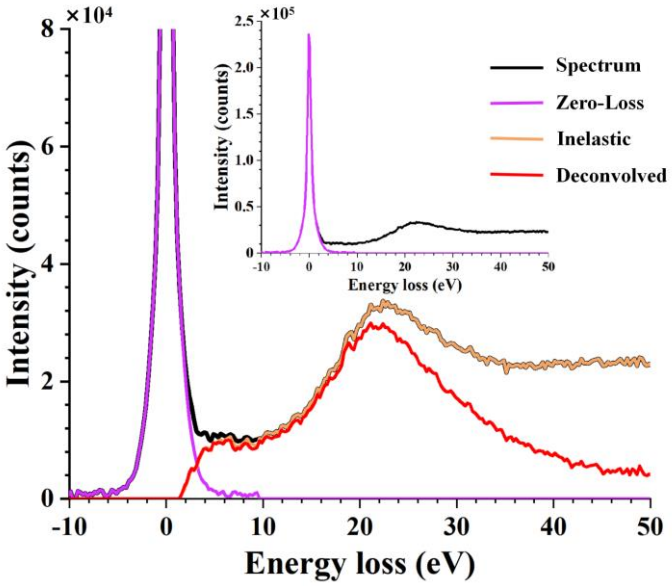

Fig. S8.

Example of the Fourier-log deconvolution of the low-loss EELS for a 100 nm *s*-PS particle. The black curve illustrates the original spectrum, while the red curve depicts the single-scattering spectrum obtained after deconvolution, as derived using Ritchie's formalism for planar surface modes. The purple line indicates the ZLP and its associated tail as removed from the EELS. The yellow line represents the spectrum after the removal of the ZLP and its tail. The inset displays a comprehensive view of the spectrum's full range. The ZLP was extracted from the low-loss EELS of the particles using a reflected-tail method, a technique proven to yield dependable results for akin aerosol particles.

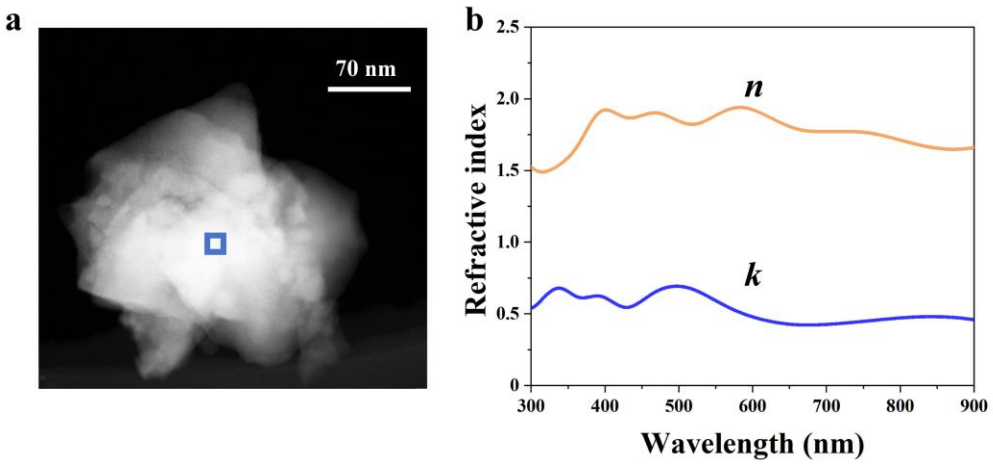

Fig. S9.

Optical properties of BC. a, TEM image shows a typical BC aggregate. **b**, Extracted *n* and *k* refractive index in the optical wavelength range from 300 to 900 nm. The refractive indices were extracted from the EELS acquired from the region marked as a blue box in the TEM image. The measurement values compare well against the fixed value of 1.88 – 0.59*i* used for modelling the optical properties of BC across the visible spectrum in climate models.

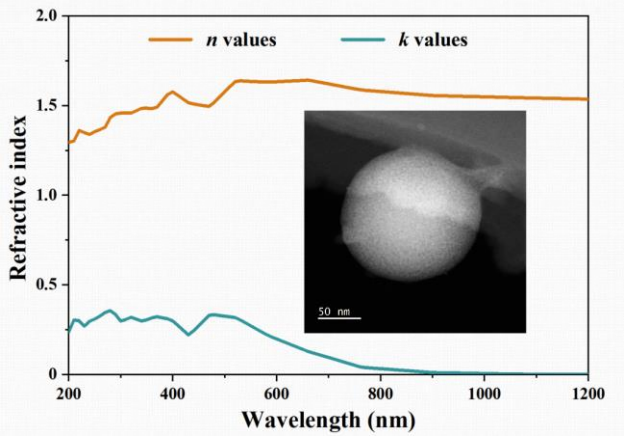

Fig. S10.

Spectral n and k values of a typical aged white MNP particle. The inset depicts the single particle from which the data were extracted. Ageing-induced yellowing causes the optical constants to progressively converge toward those of yellow MNPs.

Supplementary References

1. Wang, H. Q. *et al.* Photoaging process and mechanism of four commonly commercial microplastics. *J. Hazard. Mater.* **451**, 131151, doi:10.1016/j.jhazmat.2023.131151 (2023).
2. Duan, J. J. *et al.* Weathering of microplastics and interaction with other coexisting constituents in terrestrial and aquatic environments. *Water Res.* **196**, 117011, doi:10.1016/j.watres.2021.117011 (2021).
3. Wu, X. W. *et al.* Size-dependent long-term weathering converting floating polypropylene macro- and microplastics into nanoplastics in coastal seawater environments. *Water Res.* **242**, 120165, doi:10.1016/j.watres.2023.120165 (2023).
4. Su, J. N. *et al.* Differential photoaging effects on colored nanoplastics in aquatic environments: physicochemical properties and aggregation kinetics. *Environ. Sci. Technol.* **57**, 15656–15666, doi:10.1021/acs.est.3c04808 (2023).
5. Liu, Y. *et al.* Overcoming the fluorescent interference during Raman spectroscopy detection of microplastics. *Sci. Total Environ.* **897**, 165333, doi:10.1016/j.scitotenv.2023.165333 (2023).
6. Brahney, J. *et al.* Constraining the atmospheric limb of the plastic cycle. Proc. *Natl. Acad. Sci. U. S. A.* **118**, e2020719118, doi:10.1073/pnas.2020719118 (2021).
7. Cózar, A. *et al.* Plastic debris in the open ocean. *Proc. Natl. Acad. Sci. U. S. A.* **111**, 10239-10244, doi:10.1073/pnas.1314705111 (2014).
8. Pottinger, A. S. *et al.* Pathways to reduce global plastic waste mismanagement and greenhouse gas emissions by 2050. *Science* **386**, 1168-1173, doi:10.1126/science.adr3837 (2024).
9. Hietbrink, S. T., *et al.* Nanoplastic concentrations across the North Atlantic. *Nature* **643**, 412–416, doi:10.1038/s41586-025-09218-1 (2025).
10. Evangeliou, N. *et al.* Sources and fate of atmospheric microplastics revealed from inverse and dispersion modelling: from global emissions to deposition. *J. Hazard. Mater.* **432**, 128585, doi:10.1016/j.jhazmat.2022.128585 (2022).
11. Szopa, S. *et al.* Short-Lived Climate Forcers. In Climate Change 2021: The Physical Science Basis. Contribution of Working Group I to the Sixth Assessment Report of the Intergovernmental Panel on Climate Change [Masson-Delmotte, V. *et al.* (eds.)]. Cambridge University Press, Cambridge, United Kingdom and New York, NY, USA, pp. 817-922, doi:10.1017/9781009157896.008 (2021).
12. Li, Y. M. *et al.* Nitrogen dominates global atmospheric organic aerosol absorption. *Science* **387**, 6, doi:10.1126/science.adr4473 (2025).
13. -Schutgens, N. *et al.* AEROCOM and AEROSAT AAOD and SSA study – Part 1: Evaluation and intercomparison of satellite measurements. *Atmos. Chem. Phys.* **21,** 6895–6917, doi:10.5194/acp-21-6895-2021 (2021).
14. Myhre, G. *et al.* Radiative forcing of the direct aerosol effect from AeroCom Phase II simulations. *Atmos. Chem. Phys.* **13**, 1853–1877, doi:10.5194/acp-13-1853-2013 (2013).
15. Alexander, D. T. L. *et al.* Brown carbon spheres in East Asian outflow and their optical properties. *Science* **321**, 833-836, doi:10.1126/science.1155296 (2008).
16. Chakrabarty, R. K. *et al.* Shortwave absorption by wildfire smoke dominated by dark brown carbon. *Nat. Geosci.* **16**, 683-688, doi:10.1038/s41561-023-01237-9 (2023).